INORGANIC CHEMISTRY
FRONTIERS

CHINESE CHEMICAL SOCIETY · ROYAL SOCIETY OF CHEMISTRY

RESEARCH ARTICLE

View Article Online
View Journal | View Issue

Check for updates

Cite this: *Inorg. Chem. Front.*, 2023, **10**, 4869

Bi^{3+}/Sm^{3+} co-doped $LiTaO_3$ photochromic perovskites: an ultrafast erasable optical information storage medium†

Ruiting Zhang,[a] Yahong Jin, *[a] Yanmei Li,*[b] Haoyi Wu [a] and Yihua Hu *[a]

Received 22nd May 2023,
Accepted 10th July 2023

DOI: 10.1039/d3qi00956d

rsc.li/frontiers-inorganic

Inorganic photochromic materials hold great scientific and technological promise in the field of optical information storage due to their numerous advantages, including an extended color change duration, exceptional fatigue resistance, and robust thermal stability. However, their practical application has been hindered by relatively slow coloring and bleaching rates. In this study, we present a P-type photochromic perovskite material, $LiTaO_3$:Bi^{3+}/Sm^{3+}, with an ultra-fast optical response. $LiTaO_3$:Bi^{3+}/Sm^{3+} exhibits a rapid coloring time of approximately 25 seconds and an ultra-fast bleaching time of approximately 1 second, achieved through alternating 254 nm and 365 nm light irradiation. Notably, the photobleaching rate of $LiTaO_3$:Bi^{3+}/Sm^{3+} is currently the fastest among all reported inorganic photochromic materials. The prepared $LiTaO_3$:Bi^{3+}/Sm^{3+} material exhibits a maximum color change contrast of 26.49% and excellent fatigue resistance. The codopant Bi^{3+} plays a critical role in creating traps within the host lattice, which greatly enhances photochromism contrast and enables efficient long afterglow luminescence. These dual properties make the material suitable for dual-mode optical information storage in both bright and dark fields. Finally, the excellent optical properties of $LiTaO_3$:Bi^{3+}/Sm^{3+} are demonstrated in its application for erasable optical information storage vividly.

1. Introduction

The storage of information is the basis for the transmission of information in the dimension of time, and it is also the basis for the further synthesis, processing, accumulation and regeneration of information, which has great significance in the development of human history. In this highly informationized society, the amount of information is exploding with the development of people's lives and society, which has been a huge test and put a huge demand on information storage technology. Optical storage technology has attracted a lot of research attention due to its advantages such as sustainability, high storage density, a long storage life, non-contact reading and writing and erasing.[1–7] Under specific light irradiation conditions, photochromic materials can undergo specific chemical reactions that result in a change in the material's color or absorption peak of light. The initial state can be restored by heating or exposure to another wavelength of light.[8,9] Defining the two states before and after photochromic coloration enables the storage of information data. Inorganic photochromic materials, which exhibit reversible color changes under specific light source irradiation, possess good fatigue resistance, thermal stability, and strong mechanical properties[10–12] and are among the most promising media in the field of optical information storage applications. In recent years, many inorganic photochromic materials with excellent performance, such as $Ba(Zr_{0.16}Mg_{0.28}Ta_{0.56})O_3$: Pr^{3+}, $Ba_3MgSi_2O_8$: Pr^{3+}, $PbWO_4$:Yb^{3+}, Er^{3+}, La_4GeO_8:Eu^{2+}, Er^{3+}, $Na_{0.5}Bi_{2.5}Nb_2O_9$:Er^{3+}, Pr^{3+} and TiO_2:Yb^{3+},Er^{3+}, have been reported.[13–18] These materials combine reversible fluorescence modulation, long-afterglow luminescence, up-conversion luminescence and other luminescence characteristics based on reversible photochromism, providing a rich combination of information storage technology and media selection.

Photochromic materials can be divided into T-type and P-type, where the T-type needs to be heated back to its original state, while the P-type can only be restored to its original state only by irradiation with a different wavelength of light.[19] Recently, inorganic photochromic materials bleached by

---

[a] *School of Physics and Optoelectronic Engineering, Guangdong University of Technology, WaiHuan Xi Road, No. 100, Guangzhou, Guangdong, 510006, China. E-mail: yhjin@gdut.edu.cn, huyh@gdut.edu.cn*

[b] *School of Electronics and Electrical Engineering, Zhaoqing University, Yingbin Avenue, Duanzhou District, Zhaoqing, Guangdong, 526061, China. E-mail: 2010020017@zqu.edu.cn*

† Electronic supplementary information (ESI) available. See DOI: **https://doi.org/10.1039/d3qi00956d**

thermal stimulation have been widely reported.[14,20–23] Compared with photo-stimulation to induce bleaching, thermal stimulation has many limitations in practical applications. In practical information storage applications, materials often need to be processed into ceramics, films or other devices,[14,23–26] and in these states, thermal stimulation bleaching may cause irreversible effects on the physical properties of the devices and the surrounding environment. P-type photochromic materials can be bleached by irradiation with light of a specific wavelength, which causes little damage to the physical properties of the materials and makes the data read-out more convenient. However, the photobleaching process of P-type photochromic materials, which has been reported so far, takes a long time (>20 s), and some of them cannot even completely restore their initial state by photo-stimulation,[27–31] which greatly hinders their practical application potential. Therefore, to promote the practical application of memory storage media, new P-type photochromic materials with a fast photo-bleaching speed are necessary.

Some luminescent materials can absorb and store energy after being excited by a high-energy light source and then release the stored energy in the form of light after the removal of the excitation source to achieve long persistent luminescence for several seconds to several hours. This property is called persistent luminescence (PersL) or long afterglow.[32,33] PersL materials have attracted much attention in the fields of night vision surveillance,[34,35] anti-counterfeiting identification,[36,37] and information storage[38,39] due to their unique delayed luminescence characteristics. We envisage that if we can combine photochromic and delayed luminescence properties in a single material, it will be able to write and read data in both light and dark fields, significantly improving the applicability of information storage media. However, the photochromic process and the delayed luminescence process are two opposite reactions, where photochromism requires storing as many electrons as possible and delayed luminescence requires releasing the trapped electrons. How to introduce suitable defects into materials is a key factor. Combining the above issues and requirements, it will be very interesting and meaningful to design and develop a P-type inorganic photochromic material combining the fast light stimulation response and excellent PersL properties.

In this work, we report a new P-type inorganic photochromic material $LiTaO_3$:Bi^{3+}/Sm^{3+}. The material can achieve rapid coloring in ∼25 s and ultrafast bleaching in ∼1 s with good fatigue resistance under irradiation with 254 nm and 365 nm light, respectively. It also releases PersL luminescence and exhibits a bright orange-red afterglow after the excitation source is removed. The optical properties, reaction process, and luminescence mechanism of the material were studied and analyzed by diffuse reflectance spectroscopy (DRS), photoluminescence (PL), thermoluminescence (TL), PersL, and X-ray photoelectron spectroscopy (XPS) characterization. A flexible composite film was also prepared to demonstrate the proof-of-concept applications in the field of optical data storage.

2. Experimental section

2.1 Preparation

$LiTaO_3$ and $LiTaO_3$:0.5 mol% Sm^{3+}/x mol% Bi^{3+} (x = 0, 0.25, 0.5, 0.75, 1, 1.25, 1.5) were prepared by a traditional high-temperature solid phase method. Li_2CO_3 (Macklin, AR, 99.99%), Ta_2O_5 (Aladdin, AR, 99.99%), Sm_2O_3 (Aladdin, AR, 99.99%), and Bi_2O_3 (Aladdin, AR, 99.99%) were selected as raw materials and weighed according to the stoichiometric formula. The weighed powders were thoroughly mixed and ground in an agate mortar for one hour. Subsequently, the resulting mixtures were transferred to a tubular furnace and calcined in air at 1250 °C for six hours to obtain the powder samples.

2.2 Flexible composite film preparation

The PDMS (SYLGRD184) and curing agent were mixed and stirred in a beaker at a ratio of 15 : 1 to obtain a silica gel precursor. $LiTaO_3$:Bi^{3+}/Sm^{3+} powder was fully mixed with the silica gel precursor at a ratio of 1 : 15 and allowed to stand for 20 min to eliminate bubbles generated by stirring. A copper plate with a size of 100 × 100 mm^2 was placed on a heating table preheated to 50 °C. The mixture was then slowly poured onto the template until it completely covered the copper plate. Finally, the temperature of the heating table was slowly raised to 100 °C and held for 10 min to obtain a composite flexible film.

2.3 Sample characterization

The phase structure of the material was characterized using a D8 ADVANCE X-ray diffractometer (Bruker, Germany) with Cu Kα irradiation (λ = 1.5406 Å). The X-ray diffraction (XRD) patterns were analyzed using the Rietveld refinement method. An electron paramagnetic resonance (EPR) spectrometer (EMXplus-10/12, Bruker, Germany) was used to obtain EPR spectra at a frequency of 9.18 GHz at room temperature in air. Field-emission scanning electron microscopy (FE-SEM, Hitachi-SU8220 Instruments) was used to examine the surface micromorphology and energy-dispersive spectroscopy (EDS) elemental mapping images. DRS was conducted using a UV-visible spectrophotometer (UV-3600 Plus, Shimadzu, China). Thermal stimulation bleaching was achieved by placing the sample-loaded carrier on a pre-set temperature heating stage for heating. The light source used in the photobleaching experiment is a 365 nm laser with adjustable power. The power density of the 254 nm light source used for sample coloring is 5.73 mW cm^{-2}. The PL spectra, photoluminescence excitation (PLE) spectra, PersL spectra, and fluorescence decay curves were obtained using a fluorescence spectrophotometer (FLS980, Edinburgh Instruments). TL curves were characterized using a TL meter (SL08-L and Risø TL/OSL-DA-20) with a heating rate of 3 °C s^{-1}. XPS was conducted on an X-ray photoelectron spectrometer (Escalab 250Xi, Thermo Fisher, USA) to analyze elemental valence states.

3. Results and discussion

3.1 Phase identification and structural analysis

XRD patterns of $LiTaO_3$ and $LiTaO_3$:0.5 mol% Sm^{3+}/x mol% Bi^{3+} (x = 0, 0.25, 0.5, 0.75, 1, 1.25, 1.5) are shown in Fig. 1(a). All diffraction peaks can be well indexed to the standard card PDF#29-0836, indicating the successful incorporation of Sm^{3+} and Bi^{3+} into the $LiTaO_3$ host lattice. The (0 1 2) plane shifts towards a lower angle with the increase of Bi^{3+} doping concentration. Due to the low melting point of lithium, it is easy to volatilize and lose during high-temperature sintering, resulting in a large number of lithium vacancies $\left(V_{\mathrm{Li}}^{\bullet}\right)$ in the crystal. To maintain electrical neutrality, a small amount of tantalum is introduced to occupy some of the lithium vacancies $\left(V_{\mathrm{Li}}^{\bullet}\right)$, resulting in the formation of anti-site tantalum $\left(\mathrm{Ta}_{\mathrm{Li}}^{4+}\right)$.[40,41] In addition, oxygen vacancies may also be generated in the crystal to maintain charge balance. Fig. S1† shows the EPR spectra of the $LiTaO_3$ host lattice before and after irradiation with 254 nm light. There is a very weak isotropic electron signal from oxygen vacancies $\left(V_{\mathrm{O}}^{\bullet\bullet}\right)$ at 3510 G (g = 2.003), indicating that the density of oxygen vacancies is very low. Under 0.5 mol% Sm^{3+} doping, considering the ionic radius (Sm^{3+} CN = 6, r = 0.96 Å, Li^+ CN = 6, r = 0.76 Å, Ta^{5+} CN = 6, r = 0.64 Å) and the element valence state, Sm^{3+} ions will preferentially occupy the $V_{\mathrm{Li}}^{\bullet}$. At this time, the impact on the cell volume is not significant, and the peak position hardly shifts. After introducing Bi^{3+} (CN = 6, r = 1.03 Å,) ion doping, Sm^{3+} and Bi^{3+} compete to replace lithium vacancies and even replace anti-site defects. As the co-doping concentration increases, Bi^{3+} begins to replace the conventional Li^+ and Ta^{5+} sites, leading to lattice expansion and the diffraction peaks in XRD shifting towards lower angles.[42] The title compounds have an octahedral structure and belong to the trigonal crystal system with a space group of $R3c$. As shown in Fig. 1(b), the Li^+ and Ta^{5+} ions in the $LiTaO_3$ crystal are regularly arranged in the interstices of oxygen octahedra, forming $[LiO_6]$ and $[TaO_6]$ as the basic repeating units after occupying the interstices. In the oxygen octahedron, both Li^+ and Ta^{5+} ions are surrounded by six O^{2-} ions. In order to further analyze the structural changes of the doped samples and obtain detailed crystal information, Rietveld refinement was performed on all samples. The refinement results of $LiTaO_3$ and $LiTaO_3$:0.5 mol% Sm^{3+}/1 mol% Bi^{3+} are shown in Fig. S2† and Fig. 1(c). The refined parameters were compared with the information of the $LiTaO_3$ standard crystal and are recorded in Table 1, while the cell parameters of the other samples are recorded in Table S1.†

Table 1 Rietveld refinement parameters of $LiTaO_3$ and $LiTaO_3$:0.5 mol% Sm^{3+}/1 mol% Bi^{3+}

Parameter	$LiTaO_3$	$LiTaO_3$:0.5 mol% Sm^{3+}/1 mol% Bi^{3+}
Space group	$R3c$	$R3c$
Z	6	6
a (Å)	5.159	5.161
b (Å)	5.159	5.161
c (Å)	13.763	13.766
V (Å^3)	317.279	317.505
R_{wp} (%)	9.08	9.49
R_p (%)	7.16	7.19
χ^2	2.032	2.07

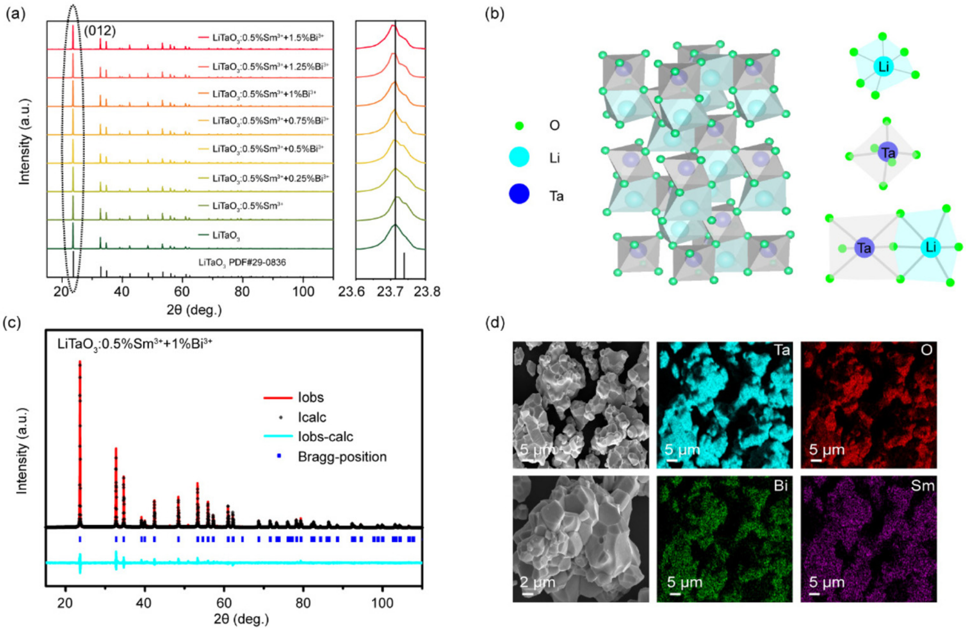

Fig. 1 (a) XRD patterns of the $LiTaO_3$ and $LiTaO_3$:0.5 mol% Sm^{3+}/x mol% Bi^{3+} (x = 0, 0.25, 0.5, 0.75, 1, 1.25, 1.5); right panel: partial enlargement of the diffraction peak of (012) in the range of 23.6°–23.8°. (b) Crystal structure of the $LiTaO_3$ host; (c) Rietveld refinement of $LiTaO_3$:0.5 mol% Sm^{3+}/1 mol% Bi^{3+}; (d) SEM and elemental EDS mapping of $LiTaO_3$:0.5 mol% Sm^{3+}/1 mol% Bi^{3+}.

The refined parameters R_{wp}, R_{p}, and χ^2 are all within a reliable range, indicating that the crystal structure of the material has not been damaged after ion doping. Compared to the host, the volume of $LiTaO_3$:0.5 mol% Sm^{3+}/1 mol% Bi^{3+} slightly increases, which is consistent with the discussed lattice expansion caused by the co-doping of Sm^{3+}/Bi^{3+} ions. Fig. 1(d) shows the SEM and elemental mapping images of $LiTaO_3$:0.5 mol% Sm^{3+}/1 mol% Bi^{3+} powder, while Fig. S3† shows the SEM images of $LiTaO_3$ and $LiTaO_3$:0.5 mol% Sm^{3+}. From the image, it can be seen that the $LiTaO_3$:0.5 mol% Sm^{3+}/1 mol% Bi^{3+} sample has a larger particle size and irregular agglomeration phenomenon, which can be attributed to the addition of Bi_2O_3 acting as a flux. The elemental mapping image also reflects the uniform distribution of doped ions Sm^{3+} and Bi^{3+} in the material.

3.2 Photochromism properties

The samples doped with Sm^{3+}/Bi^{3+} exhibit good photochromic behavior after 254 nm light irradiation. For further investigation, the DRS of all samples before and after 254 nm light irradiation were recorded, as shown in Fig. 2(a)–(c) and Fig. S4(a)–(e).† To quantify the degree of color change, ΔR was defined, which can be calculated using the formula $\Delta R = (R_0 - R_t) \times 100\%$, where R_0 and R_t are the reflectivity at 437 nm before and after UV irradiation, respectively. The non-doped and Sm^{3+} singly doped samples only show minor color changes with ΔR = 5.45% and 8.23%, respectively. However, the co-doping of Bi^{3+} significantly enhances the coloration degree to 26.49%. The photo of the sample in the illustration intuitively reflects the color change after UV irradiation. With the co-doping of Bi^{3+}, the surface of the powder can be seen changing from white to yellowish brown after UV irradiation. Fig. 2(d) shows the difference in reflectance of all samples before and after discoloration. It can be seen that the Bi^{3+} co-doped samples notably improve the photochromic performance by enhancing the coloration degree. As the concentration of Bi^{3+} doping increases, it first increases and then decreases, reaching the maximum at $x = 1$.

The reflectivity of the photochromic samples shows a strong dependence on UV irradiation time. From the illustration in Fig. 3(a), it can be observed that with the increase of 254 nm light irradiation time, the reflectivity rapidly decreases and stabilizes after ~25 s. The illustration in the lower right corner shows the variation of ΔR of the sample with irradiation time at 437 nm, indicating that ΔR has remained basically unchanged after 25 s. The photos of the sample also visually demonstrate this characteristic. We have organized and recorded the coloring rates of inorganic photochromic materials reported in recent years in Table S2.† By comparing the data in the table, it can be seen that the material has a good photochromic response speed. Interestingly, $LiTaO_3$:0.5 mol% Sm^{3+}/1 mol% Bi^{3+} can recover to its initial color under 365 nm light irradiation, indicating that it is a P-type photochromic material. To investigate the impact of light power on bleaching, the DRS of the fully colored samples were obtained after irradiation with 365 nm light with varied powers for 1 s. As shown in Fig. 3(b), high-power light is more effective for bleaching and the colored sample almost comple-

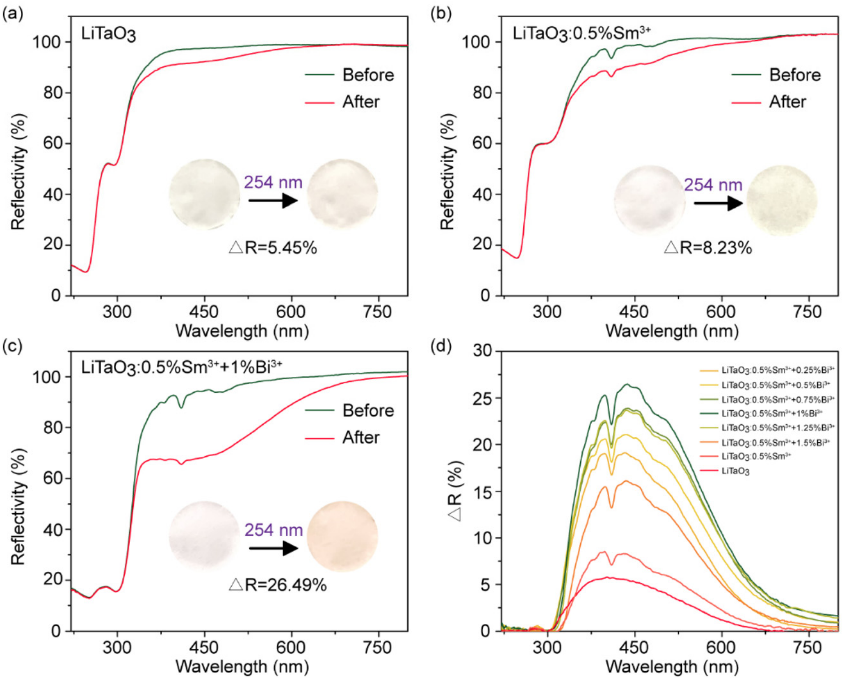

Fig. 2 DRS and color change photos before and after 254 nm light irradiation: (a) $LiTaO_3$; (b) $LiTaO_3$:0.5 mol% Sm^{3+}; (c) $LiTaO_3$:0.5 mol% Sm^{3+}/1 mol% Bi^{3+}; (d) reflectivity different spectra of $LiTaO_3$ and $LiTaO_3$:0.5 mol% Sm^{3+}/x mol% Bi^{3+} (x = 0, 0.25, 0.5, 0.75, 1, 1.25, 1.5) powders before and after 254 nm light irradiation.

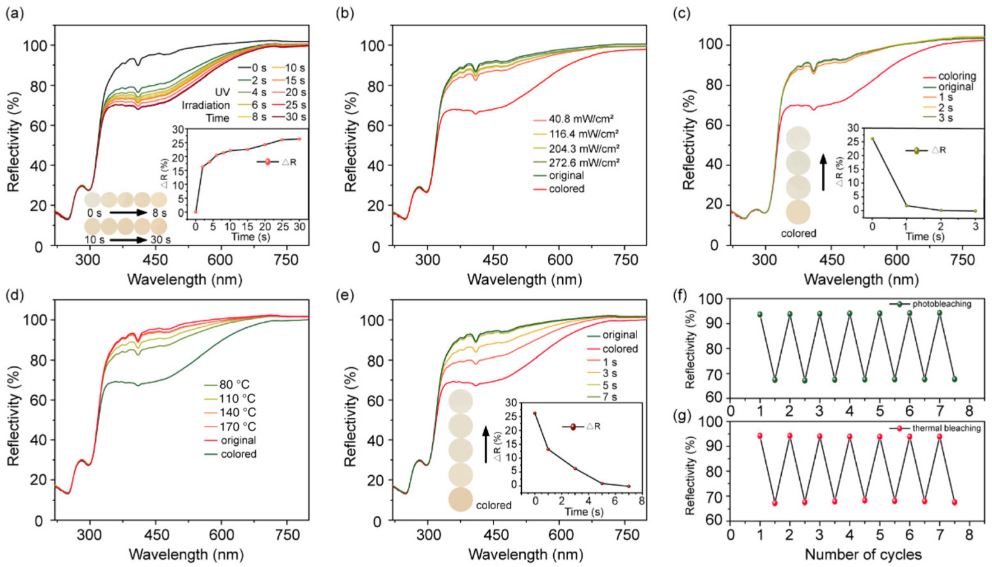

Fig. 3 (a) DRS of $LiTaO_3$:0.5 mol% Sm^{3+}/1 mol% Bi^{3+} irradiated with 254 nm light for different times. Insets show sample photos at the corresponding time during the coloring process and the relationship between the difference in reflectivity at 437 nm and irradiation time; (b) DRS of $LiTaO_3$:0.5 mol% Sm^{3+}/1 mol% Bi^{3+} under different powers of 365 nm light irradiation; (c) DRS of colored $LiTaO_3$:0.5 mol% Sm^{3+}/1 mol% Bi^{3+} under 272.6 mW cm^{-2} 365 nm light irradiation for different times. Insets show sample photos at the corresponding time during the bleaching process and the relationship between the difference in reflectivity at 437 nm and irradiation time; (d) DRS of colored $LiTaO_3$:0.5 mol% Sm^{3+}/1 mol% Bi^{3+} heated at different temperatures for 5 s; (e) DRS of colored $LiTaO_3$:0.5 mol% Sm^{3+}/1 mol% Bi^{3+} heated at 170 °C for different times. Insets show sample photos at the corresponding time during the bleaching process and the relationship between the difference in reflectivity at 437 nm and irradiation time; (f) changes in reflectivity at 437 nm under alternating irradiation at 254 nm and 365 nm; (g) changes in reflectivity at 437 nm under alternating effects of 254 nm light irradiation and 170 °C heating.

tely returns to its initial state as the power approaches 272.6 mW cm^{-2}. Subsequently, 365 nm light (272.6 mW cm^{-2}) was used as the bleaching light source to measure its bleaching rate. As shown in Fig. 3(c), the reflectivity of the sample almost returns to its initial state within ~1 s and completely recovers to its original position after 2 s, demonstrating an ultrafast bleaching speed. The bleaching speed of ~1 s is the fastest so far compared with the previously reported results summarized in Table S3,† which greatly improves the application potential in repeatable erasable information storage. Besides, $LiTaO_3$:0.5 mol% Sm^{3+}/1 mol% can also be bleached through thermal stimulation. DRS was conducted at different heating temperatures for 5 s to observe the effect of temperature on the bleaching effect. As depicted in Fig. 3(d), a higher temperature leads to faster recovery of the reflectance and the DRS almost recovers to its initial level at 170 °C. Fig. 3(e) shows the reflectivity at 170 °C for different heating times, showing that the colored sample can be completely bleached after 7 s of heating. Fatigue resistance is one of the important properties of inorganic photochromic materials. Therefore, the reflectivity of $LiTaO_3$:0.5 mol% Sm^{3+}/1 mol% at 437 nm was tested for 7 cycles by alternative 254 nm and 365 nm light irradiation/heating treatment at 170 °C. As shown in Fig. 3(f) and (g), $LiTaO_3$:0.5 mol% Sm^{3+}/1 mol% exhibits excellent fatigue resistance. Above all, good reversibility, fast coloration rate, ultrafast photobleaching speed, and excellent fatigue resistance have been achieved in $LiTaO_3$:0.5 mol% Sm^{3+}/1 mol%.

3.3 PersL properties in $LiTaO_3$:Sm^{3+}/Bi^{3+}

After 30 s of irradiation with 254 nm light, strong orange red PersL was observed in $LiTaO_3$:Sm^{3+}/Bi^{3+} powder. Therefore, the afterglow spectrum of $LiTaO_3$:0.5 mol% Sm^{3+}/x mol% Bi^{3+} (x = 0, 0.25, 0.5, 0.75, 1, 1.25, 1.5) samples was obtained, as shown in Fig. 4(a). As a reference, the excitation and emission spectra of $LiTaO_3$:0.5 mol% Sm^{3+}/1 mol% Bi^{3+} were obtained and are recorded in Fig. S5.† Under monitoring at 648 nm, an excitation peak composed of two sub-peaks was observed in the range of 220–340 nm, which were attributed to the charge transfer band of the host and the $^1S_0 \rightarrow {}^3P_1$ transition of Bi^{3+}.[31,41] The sharp peaks in the range of 340–510 nm were attributed to the transitions between $^6H_{5/2} \rightarrow {}^6H_{13/2}$, $^6H_{5/2} \rightarrow {}^4D_{3/2}$, $^6H_{5/2} \rightarrow {}^6P_{7/2}$, $^6H_{5/2} \rightarrow {}^4F_{7/2}$ and $^6H_{5/2} \rightarrow {}^4I_{13/2}$. Under excitation at 409 nm, the orange red emission peak of Sm^{3+} is displayed in the range of 550–750 nm. The peaks at 566 nm, 605 nm, 648 nm, and 709 nm are attributed to the energy-level transitions of $^4G_{5/2} \rightarrow {}^6H_{5/2}$, $^4G_{5/2} \rightarrow {}^6H_{7/2}$, $^4G_{5/2} \rightarrow {}^6H_{9/2}$, and $^4G_{5/2} \rightarrow {}^6H_{11/2}$, respectively.[43] The afterglow spectra in Fig. 4(a) match well with the emission spectrum of Sm^{3+}, indicating the origin of orange red afterglow from Sm^{3+} ions. With the co-doping of Bi^{3+} ions, the PersL intensity is significantly enhanced, reaching its maximum at x = 1. The afterglow decay curves of the co-doped samples were also recorded. As shown in Fig. 4(b), it can be seen that the afterglow intensity decreases rapidly within the first 2.5 min and then gradually

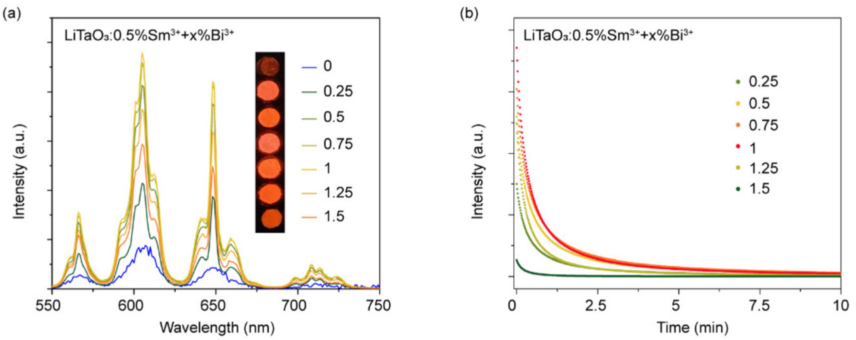

Fig. 4 (a) PersL spectra of LiTaO$_3$:0.5 mol% Sm^{3+}/*x* mol% Bi^{3+} (*x* = 0, 0.25, 0.5, 0.75, 1, 1.25, 1.5) powder irradiated at 254 nm for 30 s. Insets: afterglow photos of the corresponding samples; (b) the afterglow decay curves of Sm^{3+}/Bi^{3+} co-doped samples at room temperature after being irradiated with 254 nm light for 30 s.

stabilizes. The intensity of the afterglow decay curves exhibits the same change trend as that of the afterglow spectrum, approaching the maximum at $x = 1$. The afterglow photos of the LiTaO$_3$:0.5 mol% Sm^{3+}/1 mol% Bi^{3+} sample after being excited by 254 nm light and placed in a dark field for different times are recorded in Fig. S6.† Even after 120 min, a faint red luminescence can be still observed.

3.4 Thermoluminescence

In general, defects in inorganic materials are the main cause of photochromism and PersL. TL is an efficient tool and usually used for the study of traps, including the trap depth and distribution.[44,45] Fig. 5(a) shows the TL spectra of the host and LiTaO$_3$:0.5 mol% Sm^{3+}/*x* mol% Bi^{3+} (*x* = 0, 0.25, 0.5, 0.75, 1, 1.25, 1.5) after 30 s of exposure to 254 nm light. It was observed that the TL peak intensities of LiTaO$_3$ and LiTaO$_3$:0.5 mol% Sm^{3+} samples were very weak in the range of 50–150 °C. After the introduction of Bi^{3+} ion doping, the trap density of the co-doped sample significantly increased in the temperature range of 60–140 °C. As the co-doping concentration of Bi^{3+} ions increases, the TL peak intensity first increases and then decreases, reaching its maximum at $x = 1$. Under the excitation of ultraviolet light, the traps capture electrons, and after the light source is removed, the traps spon-

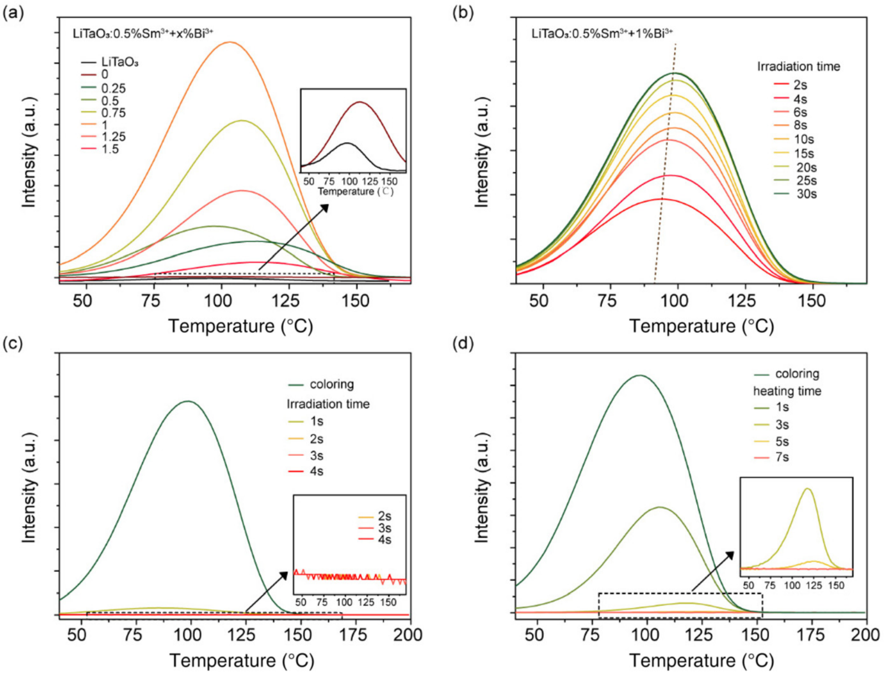

Fig. 5 (a) TL spectra of LiTaO$_3$ and LiTaO$_3$:0.5 mol% Sm^{3+}/*x* mol% Bi^{3+} (*x* = 0, 0.25, 0.5, 0.75, 1, 1.25, 1.5) samples irradiated with 254 nm light for 30 s; (b) TL spectra of LiTaO$_3$:0.5 mol% Sm^{3+}/1 mol% Bi^{3+} samples irradiated at 254 nm for different times; (c) TL spectra of colored LiTaO$_3$:0.5 mol% Sm^{3+}/1 mol% Bi^{3+} samples after 365 nm photobleaching for different times; (d) TL spectra of colored LiTaO$_3$:0.5 mol% Sm^{3+}/1 mol% Bi^{3+} samples after heating at 170 °C for different times.

taneously release electrons and produce afterglow luminescence. The emission spectrum of the $LiTaO_3$:0.5 mol% Sm^{3+}/1 mol% Bi^{3+} sample during TL measurements was recorded, as shown in Fig. S7.† The observed emission spectrum in the figure matches well with the Sm^{3+} luminescence, indicating that Sm^{3+} serves as a composite luminescent center. The higher trap density is more favorable for afterglow luminescence. The PersL spectrum in Fig. 4(a) also confirms this point. In addition, a high trap density is more favorable for capturing electrons excited by 254 nm light. After being captured, the electrons form a composite center, namely a color center. The increase in the number of color centers and their absorption of specific light leads to an increase in the degree of color change in the material. Combining Fig. 5(a) and 2(d), it can be concluded that the increase in trap density level after co-doping significantly enhances the photochromic effect. Besides, in previous reports by Lyu *et al.*, Bi^{3+} can introduce an electron capture center of 0.8 ± 0.5 eV depth in the $LiTaO_3$ host.[31,46] For the TL peak of 0.5 mol% Sm^{3+}/x mol% Bi^{3+} samples, the corresponding trap depth was calculated using Chen's formula: $E = \frac{T_m}{500}$, where T_m is the temperature of the TL peak.[47] The calculated trap depths of $LiTaO_3$:0.5 mol% Sm^{3+}/x mol% Bi^{3+} (x = 0.25, 0.5, 0.75, 1, 1.25, 1.5) were 0.772 eV, 0.741 eV, 0.761 eV, 0.753 eV, 0.761 eV, and 0.749 eV, respectively. In the study by Maldiney *et al.*, traps within this depth range were beneficial for PersL.[48] This suggests that the trap depth in the co-doped samples provides strong support for their PersL. The TL spectra of $LiTaO_3$:0.5 mol% Sm^{3+}/1 mol% Bi^{3+} were characterized after being irradiated with 254 nm light for different times to understand the process of carrier capture, as shown in Fig. 5(b). As the irradiation time is prolonged, the TL intensity of the sample gradually increases and reaches stability at 30 s. During the charging process, the TL curves shift to higher temperature, indicating that electrons first fill shallow traps and then deep traps. However, the storage of charge carriers in traps is not stable. The TL curves were tested at different delay times after being irradiated with 254 nm light for 30 s, as shown in Fig. S8(a).† After 240 min, the shallow trap almost disappeared, while the deep trap still had weaker peaks, which was caused by the spontaneous escape of the captured carriers in the trap. Fig. S8(b)† shows the DRS and the corresponding surface photos of $LiTaO_3$:0.5 mol% Sm^{3+}/1 mol% Bi^{3+} at different delay times after being irradiated with 254 nm light for 30 s. With the increase of delay time, the reflectance of the samples gradually recovered to the initial value, showing a consistent rule with the TL spectrum. However, photochromism involves trapping electrons as color centers, while PersL involves electrons being released by traps and returning to the luminescent center, which is an opposite process. As the afterglow luminescence continues, the charge carriers are gradually released, resulting in a gradual decrease in photochromic contrast. Light or heat stimulation can accelerate the release process of carriers in defects. Therefore, the TL curves of the irradiated samples were characterized at different times under 365 nm light or 170 °C thermal stimulation and are recorded in Fig. 5(c) and (d). Under the irradiation with 365 nm light, the TL peak almost disappears after about 1 s, indicating that the 365 nm light strongly promotes the escape of trapped carriers. Similarly, under stimulation at 170 °C, the charge carriers in the trap were rapidly released and it was completely emptied within 7 s.

3.5 The mechanism of photochromism and PersL

In order to discuss the photochromic and afterglow processes of $LiTaO_3$:Sm^{3+}/Bi^{3+}, a schematic diagram for the illustration of the mechanism is proposed. As shown in Fig. 6, the melting point of lithium is around 180 °C, so it is prone to volatiliz-

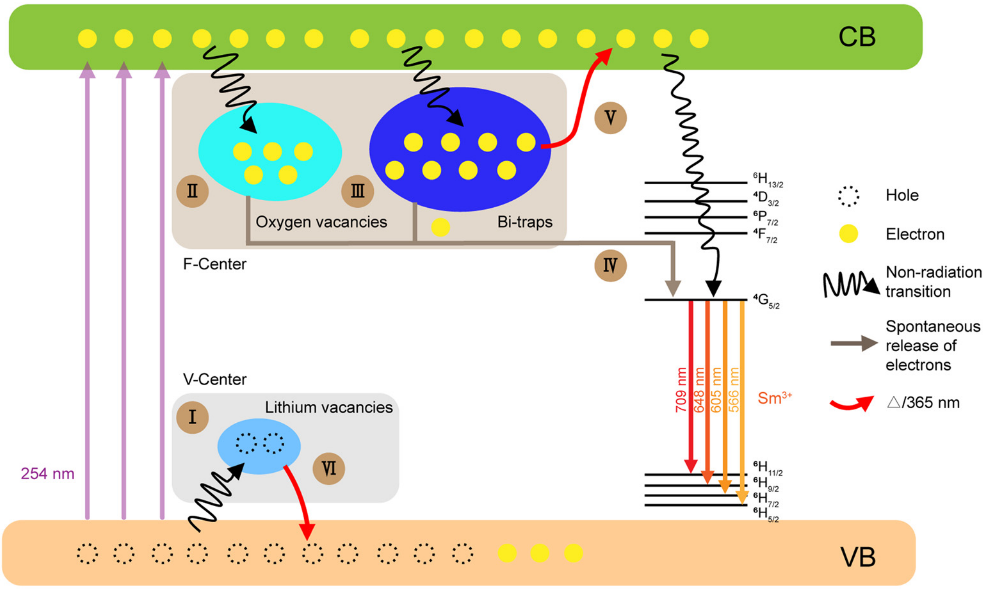

Fig. 6 Schematic diagram of the mechanism of photochromism and PersL processes.

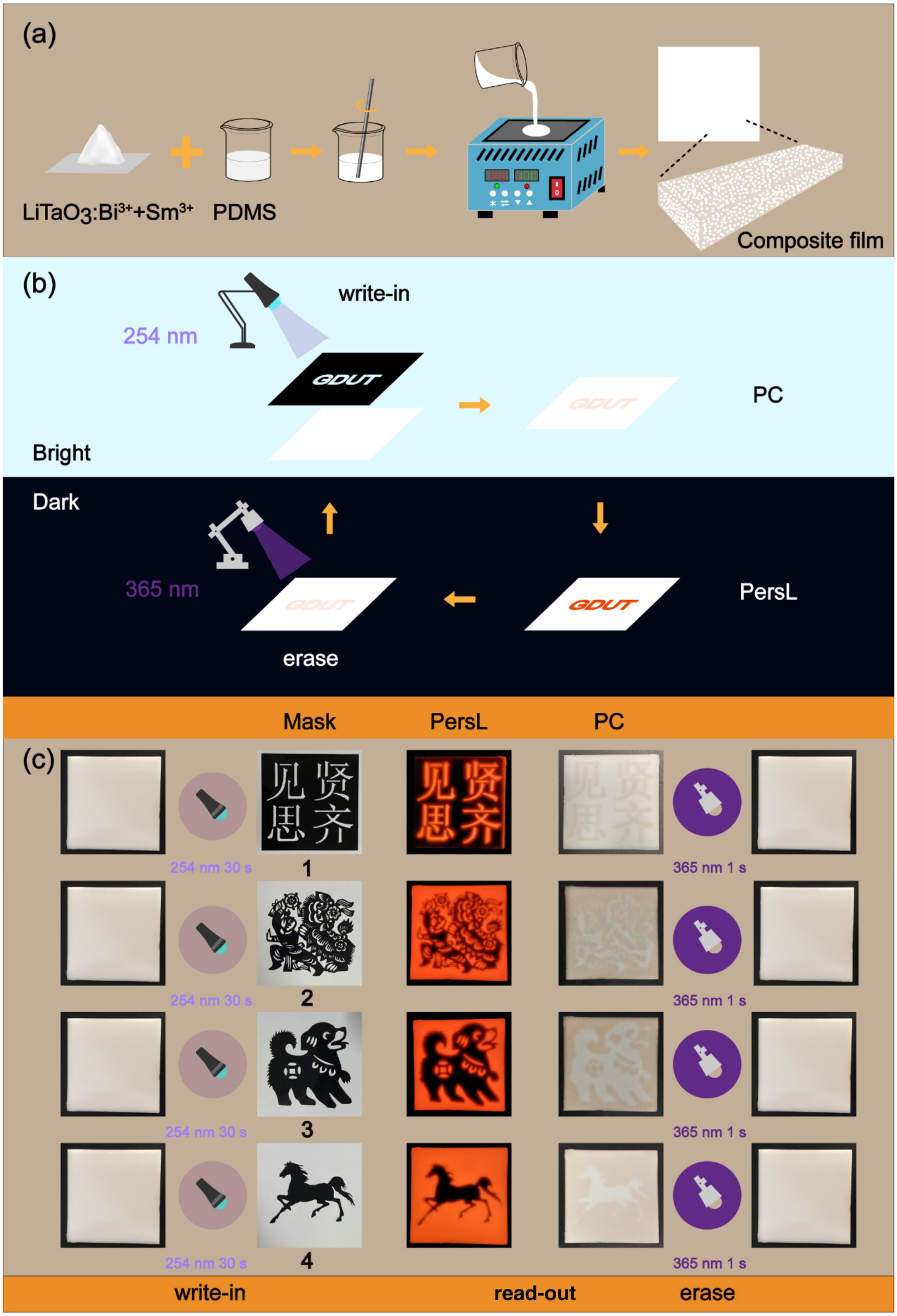

Fig. 7 (a) The fabrication process of composite flexible film was demonstrated; (b) the process of optical information writing and erasing of flexible composite films and information reading under bright and dark field conditions is demonstrated; (c) by alternating 254 nm/365 nm light irradiation, text or image information is written or erased into the thin film using different masks. Mask 1 is the text of a Chinese idiom, and masks 2–4 are the patterns of "lion dance paper cuttings", "dog" and "horse", respectively.

ation and loss during high-temperature sintering, which will generate a large number of $V_{\mathrm{Li}}^{\bullet}$ in $LiTaO_3$. When Sm^{3+} and Bi^{3+} are doped into the $LiTaO_3$ crystal, they will compete to replace $V_{\mathrm{Li}}^{\bullet}$. When the doping concentration increases to a certain extent, they will start to replace conventional Li^+ and Ta^{5+}, and these unequal substitutions will cause charge imbalance within the crystal, resulting in the corresponding $\left(V_{\mathrm{O}}^{\bullet\bullet}\right)$ for charge compensation. From the TL curve, it can be concluded that the co-doping of Bi^{3+} ions introduces a trap with a level of approximately 0.75–0.77 eV in the crystal. According to the DRS of $LiTaO_3$, the band gap (E_g) was calculated to be 4.78 eV using the formula. The calculation process is recorded in Fig. S9† and explained in the ESI accordingly†. Based on the traps introduced by Bi^{3+} (Bi-traps), they are located near the conduction band (CB), which can function as electron capture traps. Upon excitation with 254 nm light, the charge carriers in the valence band (VB) absorb energy and transit to the CB, leaving behind hole carriers in the VB. Some of the hole carriers will be captured by $V_{\mathrm{Li}}^{\bullet}$ near the VB and recombine into V color centers (process I). Process I generates only a small number of V-centers, which have a weak impact on the color change of the crystal. The electrons that enter the CB will move towards lower energy states in a non-radiative transition. During this process, electrons will be captured by $\left(V_{\mathrm{O}}^{\bullet\bullet}\right)$ defects and Bi-traps in the crystal to form F color centers, which are processes II and III, respectively. The trap density in this part dominates the material, resulting in a significant number of F-centers being formed. The selective absorption of visible light by color centers leads to a change in the color of the crystal, known as photochromism. The process of filling electrons in the photochromic process of Bi-trap is given in Fig. 5(b). To investigate the changes in $\left(V_{\mathrm{O}}^{\bullet\bullet}\right)$, the O_{1s} signal of the sample before and after 254 nm light irradiation was characterized by XPS, as shown in Fig. S10.† The O_{1s} signal is well fitted into three peaks, which correspond to lattice oxygen (530.1 eV), $V_{\mathrm{O}}^{\bullet\bullet}$ (531.7 eV), and absorbed oxygen (533.5 eV).[49–52] Following irradiation, the proportion of the fitted area for $V_{\mathrm{O}}^{\bullet\bullet}$ increased from 42.19% to 45.86%, indicating a rise in the $V_{\mathrm{O}}^{\bullet\bullet}$ content within the crystal, which is conducive to photochromism. The emission of Sm^{3+} mainly comes from the transition between the energy of $^4G_{5/2} \rightarrow {}^6H_{i/2}$ (i = 5, 7, 9, 11). According to the formula $E = h\frac{c}{\lambda}$, the energy level bandwidth from $^6H_{5/2}$ to $^4G_{5/2}$ can be calculated to be approximately 2.2 eV, where h is the Planck constant, c is the speed of light, and λ is the wavelength of light. By comparison, it can be concluded that the above energy levels are located close to the VB in the bandgap, below the $\left(V_{\mathrm{O}}^{\bullet\bullet}\right)$ and Bi-trap positions. Under thermal agitation, the captured electrons will spontaneously escape from the trap. The escaped electrons will move to the $^4G_{5/2}$ energy level of Sm^{3+} and generate luminescence through energy-level transitions (process IV), which is the mechanism of PersL generation. As process IV continues, the number of F-centers will decrease, causing the crystal color to slowly return to its initial state. In addition, 365 nm light irradiation/thermal stimulation can promote the release of trapped electrons in the F-centers (process V). The excited electrons will return to the CB and then move to the high energy levels of Sm^{3+} in the bandgap through non-radiative transitions. After relaxation to the $^4G_{5/2}$ energy level, luminescence is generated through radiative transitions and eventually returns to the VB. The temperature range of trap distribution is wide, with the majority of traps concentrated in shallow levels, which facilitates the release of trapped electrons. Consequently, when stimulated by an appropriate external light source, the process of electron escape is accelerated, resulting in the rapid fading of the material. Simultaneously, the V-centers undergo decomposition and the holes within it return to the valence band (process VI). The schematic diagram in Fig. 6 visually displays the above discussion on photochromism and PersL.

3.6 Rewritable optical information storage applications

Flexible composite films containing $LiTaO_3$:Sm^{3+}/Bi^{3+} phosphors were prepared to verify their potential for optical information storage. The preparation process for the thin films is illustrated in Fig. 7(a), with a detailed description provided in the Experimental section. Fig. 7(b) demonstrates the use of the flexible composite films for storing optical information. The process involves covering the hollow mask carrying the designed information on the film, followed by 30 s of 254 nm light irradiation. The mask is then removed to reveal the information generated by photochromism under a bright field. The pattern information emits bright orange-red light in a dark field owing to the PersL from $LiTaO_3$:Sm^{3+}/Bi^{3+}. The recorded information in the thin film can be quickly erased by 365 nm illustration for 1 s. Videos were used to demonstrate the excellent light response speed of the $LiTaO_3$:Sm^{3+}/Bi^{3+} material in the process of writing and erasing of the designed letters, as presented in ESI Videos 1 and 2.† The recording and erasing of the actual text and pattern information is shown in Fig. 7(c). On a thin film with dimensions of 100 × 100 mm^2, mask 1 was used to record the Chinese idiom "Emulate those better than oneself". Due to the excellent PersL intensity and photochromic contrast of $LiTaO_3$:Sm^{3+}/Bi^{3+}, the text on the composite film exhibits ideal resolution under both dark field and bright field conditions. With the help of masks 2–4, the writing and erasing of a series of patterns such as "lion dance paper cuttings", "dog", and "horse" were realized. The results demonstrate the application potential of the inorganic photochromic materials $LiTaO_3$:Sm^{3+}/Bi^{3+} as erasable optical information storage media.

4. Conclusions

In summary, we prepared a novel P-type inorganic photochromic material by co-doping Bi^{3+}/Sm^{3+} in $LiTaO_3$ using a traditional high-temperature solid-state method. $LiTaO_3$:Sm^{3+}/Bi^{3+} achieved a coloring speed of ∼25 s and a bleaching speed of ∼1 s under the alternating action of 254 nm and 365 nm light, and the photobleaching speed is the fastest among the reported inorganic photochromic materials. After irradiation with 254 nm light, $LiTaO_3$:Sm^{3+}/Bi^{3+} demonstrated a maximum photochromic contrast of 26.49% and exhibited excellent fatigue resistance. In $LiTaO_3$ crystals, Sm^{3+} acts as the luminescent center, while the co-doping of Bi^{3+} introduces new traps that give the material excellent delayed luminescence properties. The photochromism and afterglow luminescence were investigated by means of characterization methods such as DRS, TL, and XPS, and a mechanism diagram was constructed to provide a reasonable explanation for their processes. The combination of photochromic and afterglow properties makes it possible for materials to be applied to information storage and reading in both light and dark fields. A flexible film was prepared to validate this idea. It is hoped that this work will promote the development of inorganic photochromic materials for optical information storage by improving their photobleaching speed.

Conflicts of interest

The authors declare no conflict of interest.

Data availability

The data that support the findings of this study are available from the corresponding author upon reasonable request.

Acknowledgements

The authors acknowledge the financial support from the National Natural Science Foundation of China (No. 51972065 & 51802045) and the Guangzhou Basic and Applied Basic Research Project (202102020871). We also would like to thank the Analysis and Test Center of Guangdong University of Technology for the XRD, SEM and XPS analyses.

References

1 H. Wu, M. Wang, L. Huai, W. Wang, J. Zhang and Y. Wang, Optical storage and operation based on photostimulated luminescence, *Nano Energy*, 2021, **90**, 106546.

2 X. Lin, K. Deng, H. Wu, B. Du, B. Viana, Y. Li and Y. Hua, Photon energy conversion and management in $SrAl_{12}O_{19}$: Mn^{2+}, Gd^{3+} for rewritable optical information storage, *Chem. Eng. J.*, 2021, **420**, 129844.

3 Y. Xie, Y. Song, G. Sun, P. Hu, A. Bednarkiewicz and L. Sun, Lanthanide-doped heterostructured nanocomposites toward advanced optical anti-counterfeiting and information storage, *Light: Sci. Appl.*, 2022, **11**, 150.

4 Y. Wang, D. Chen, Y. Zhuang, W. Chen, H. Long, H. Chen and R. Xie, $NaMgF_3$:Tb^{3+}@$NaMgF_3$ nanoparticles containing deep traps for optical information storage, *Adv. Opt. Mater.*, 2021, 2100624.

5 T. Xu, S. Guo, W. Qi, S. Li, M. Xu and W. Wang, Organic transistor nonvolatile memory with three-level information storage and optical detection functions, *ACS Appl. Mater. Interfaces*, 2020, **12**, 21952–21960.

6 D. Liu, L. Yuan, Y. Jin, H. Wu, Y. Lv, G. Xiong, G. Ju, L. Chen, S. Yang and Y. Hua, Tailoring multidimensional traps for rewritable multilevel optical data storage, *ACS Appl. Mater. Interfaces*, 2019, **11**, 35023–35029.

7 H. Wang, Y. Lei, L. Wang, M. Sakakura, Y. Yu, C. Shayeganrad and P. Kazansky, 100-layer error-free 5D optical data storage by ultrafast laser nanostructuring in glass, *Laser Photonics Rev.*, 2022, **16**, 2100563.

8 R. Exelby and R. Grintetr, Phototropy (or Photochromism), *Chem. Rev.*, 1965, **65**, 247–260.

9 G. H. Brown, Photochromism, *Tech. Chem.*, 1971, 853.

10 F. Yang, B. Jia, T. Wei, C. Zhao, Q. Zhou, Z. Li, M. Du, M. Wang, Y. Liu and C. Xie, Reversible regulation of upconversion luminescence in new photochromic ferroelectric materials: $Bi_{4-x}Er_xTi_3O_{12}$ ceramics, *Inorg. Chem. Front.*, 2019, **6**, 2756.

11 H. Sun, Y. Zhang, J. Liu, D. Peng, Q. Zhang and X. Hao, Reversible upconversion switching for Ho/Yb codoped (K, Na)NbO_3 ceramics with excellent luminescence readout capability, *J. Am. Ceram. Soc.*, 2018, **101**, 5659–5674.

12 L. Yuan, Y. Jin, Y. Su, H. Wu, Y. Hu and S. Yang, Optically stimulated luminescence phosphors: Principles, applications, and prospects, *Laser Photonics Rev.*, 2020, 2000123.

13 W. Tang, C. Zuo, C. Ma, Y. Wang, Y. Li, X. Yuan, E. Wang, Z. Wen and Y. Cao, Designing photochromic materials with high photochromic contrast and large luminescence modulation for hand-rewritable information displays and dual-mode optical storage, *Chem. Eng. J.*, 2022, **435**, 134670.

14 W. Tang, C. Zuo, C. Ma, C. Chang, F. Dang, H. Liu, Y. Li, X. Yuan, Z. Wen, L. Wu and Y. Cao, Rapid high-contrast reversible coloration of $Ba_3MgSi_2O_8$:Pr^{3+} photochromic materials for rewritable light-printing, *J. Mater. Chem. C*, 2022, **10**, 18375.

15 X. Bai, Z. Yang, Y. Zhan, Z. Hu, Y. Ren, M. Li, Z. Xu, A. Ullah, I. Khan, J. Qiu, Z. Song, B. Liu and Y. Wang, Novel strategy for designing photochromic ceramic: Reversible upconversion luminescence modification and optical information storage application in the $PbWO_4$:Yb^{3+}, Er^{3+} photochromic ceramic, *ACS Appl. Mater. Interfaces*, 2022, **12**, 21936–21943.

16 P. Pei, R. Wei, B. Wang, J. Su, Z. Zhang and W. Liu, An advanced tunable multimodal luminescent La_4GeO_8: Eu^{2+}, Er^{3+} phosphor for multicolor anticounterfeiting, *Adv. Funct. Mater.*, 2021, **31**, 2102479.

17 J. Gong, P. Du, W. Li, G. Yuan, X. Mao and L. Luo, The enhancement of photochromism and luminescence modulation properties of ferroelectric ceramics via chemical and physical strategies, *Laser Photonics Rev.*, 2022, **16**, 2200170.

18 A. A. Haider, Y. Cun, X. Bai, Y. Zi, J. Qiu, Z. Song, A. Huang and Z. Yang, Anti-counterfeiting applications by photochromism induced modulation of reversible upconversion luminescence in TiO_2:Yb^{3+}, Er^{3+} ceramic, *J. Mater. Chem. C*, 2022, **10**, 6243–6251.

19 A. Bianco, S. Perissinotto, M. Garbugli, G. Lanzani and C. Bertarelli, Control of optical properties through photochromism: a promising approach to photonics, *Laser Photonics Rev.*, 2011, **5**, 711–736.

20 Q. Du, J. Ueda, R. Zheng and S. Tanabe, Photochromism and long persistent luminescence in Pr^{3+}-doped garnet transparent ceramic via UV or blue light up-conversion charging, *Adv. Opt. Mater.*, 2023, 2202612.

21 Z. Yang, J. Hu, D. V. d. Heggen, M. Jiao, A. Feng, H. Vrielinck, P. F. Smet and D. Poelman, A versatile photochromic dosimeter enabling detection of X-ray, ultraviolet, and visible photons, *Laser Photonics Rev.*, 2023, 2200809.

22 F. Yu, P. Wang, J. Lin, P. Zhou, Y. Ma, X. Wu, C. Lin, C. Zhao, M. Gao and Q. Zhang, $(K_{0.5}Na_{0.5})NbO_3$-based photochromic transparent ceramics for high-security dynamic anti-counterfeiting and optical storage applications, *J. Lumin.*, 2022, **252**, 119345.

23 Y. Mu, J. Yao, X. Wan, X. Mao and L. Luo, The integration of multi-luminescence in Sr_2SnO_4:xEr^{3+}/Sm^{3+}, *J. Alloys Compd.*, 2022, **909**, 164801.

24 X. Li, H. Lin, S. Lin, P. Li, P. Wang, J. Xu, Y. Cheng, Q. Zhang and Y. Wang, Rare-earth-ion doped $Bi_{1.5}ZnNb_{1.5}O_7$ photochromics: A fast self-recoverable optical storage medium for dynamic anti-counterfeiting with high security, *Laser Photonics Rev.*, 2023, 2200734.

25 Y. Zhou, A. Huang, S. Ji, H. Zhou, P. Jin and R. Li, Scalable preparation of photochromic composite foils with excellent reversibility for light printing, *Chem. – Asian J.*, 2018, **13**, 457–462.

26 Z. Hu, X. Huang, Z. Yang, J. Qiu, Z. Song, J. Zhang and G. Dong, Reversible 3D optical data storage and information encryption in photo-modulated transparent glass medium, *Light: Sci. Appl.*, 2021, **10**, 140.

27 Y. Wang, X. Yuan, Y. Cao and C. Ma, Multiple anti-counterfeiting strategy by integrating up-conversion, down-shifting luminescence, phosphorescence and photochromism into $NaYTiO_4$: Bi/Er phosphors, *J. Mater. Sci. Technol.*, 2022, **130**, 219–226.

28 L. Sun, B. Wang, G. Xing, C. Liang, W. Ma and S. Yang, Bi-induced photochromism and photo-stimulated luminescence with fast photochromic response for multi-mode dynamic anti-counterfeiting and optical information storage, *Chem. Eng. J.*, 2023, **455**, 140752.

29 L. Shen, T. Wei, Y. Shi, X. Wang, L. Wu, J. Cui, T. Zhang, H. Yu and Z. Li, Light–heat and light–light dual-controlled upconversion luminescence and photochromic processes in Er-activated $Bi_7Ti_4NbO_{21}$ for Optical Information Storage, *ACS Appl. Elecrton. Mater.*, 2022, **4**, 776–786.

30 Z. Yang, J. Du, L. I. D. J. Martin, A. Feng, E. Cosaert, B. Zhao, W. Liu, R. V. Deun, H. Vrielinck and D. Poelman, Designing photochromic materials with large luminescence modulation and strong photochromic efficiency for dual-mode rewritable optical storage, *Adv. Opt. Mater.*, 2021, **9**, 2100669.

31 T. Lyu, P. Dorenbos, C. Li and Z. Wei, Wide range X-ray to infrared photon detection and energy storage in $LiTaO_3$:Bi^{3+},Dy^{3+} perovskite, *Laser Photonics Rev.*, 2022, **16**, 2200055.

32 L. Liang, J. Chen, K. Shao, X. Qin, Z. Pan and X. Liu, Controlling persistent luminescence in nanocrystalline phosphors, *Nat. Mater.*, 2023, **22**, 289.

33 S. Wu, Y. Li, W. Ding, L. Xu, Y. Ma and L. Zhang, Recent advances of persistent luminescence nanoparticles in bioapplications, *Nano-Micro Lett.*, 2020, **12**, 70.

34 J. Ueda, S. Miyano and S. Tanabe, Formation of deep electron traps by Yb^{3+} codoping leads to super-long persistent luminescence in Ce^{3+}-doped yttrium aluminum gallium garnet phosphors, *ACS Appl. Mater. Interfaces*, 2018, **10**, 20652–20660.

35 M. Li, Y. Jin, L. Yuan, B. Wang, H. Wu, Y. Hu and F. Wang, Near-infrared long afterglow in Fe^{3+}-activated Mg_2SnO_4 for self-sustainable night vision, *ACS Appl. Mater. Interfaces*, 2023, **15**, 13186–13194.

36 S. Tian, P. Feng, S. Ding, Y. Wang and Y. Wang, A color-tunable persistent luminescence material $LiTaO_3$:Pr^{3+} for dynamic anti-counterfeiting, *J. Alloys Compd.*, 2022, **899**, 163325.

37 C. Wang, Y. Jin, J. Zhang, X. Li, H. Wu, R. Zhang, Q. Yao and Y. Hu, Linear charging-discharging of an ultralong UVA persistent phosphor for advanced optical data storage and wide-wavelength-range detector, *Chem. Eng. J.*, 2023, **453**, 139558.

38 Y. Zhuang, D. Chen, W. Chen, W. Zhang, X. Su, R. Deng, Z. An, H. Chen and R. Xie, X-ray-charged bright persistent luminescence in $NaYF_4$:Ln^{3+}@$NaYF_4$ nanoparticles for multidimensional optical information storage, *Light: Sci. Appl.*, 2021, **10**, 132.

39 Z. Zhou, X. Wang, X. Yi, H. Ming, Z. Ma and M. Peng, Rechargeable and sunlight-activated $Sr_3Y_2Ge_3O_{12}$:Bi^{3+} UV–Visible-NIR persistent luminescence material for night-vision signage and optical information storage, *Chem. Eng. J.*, 2021, **421**, 127820.

40 L. Li, Y. Li and X. Zhao, Hybrid density functional theory insight into the stability and microscopic properties of Bi-doped $LiNbO_3$: Lone electron pair effect, *Phys. Rev. B*, 2017, **96**, 115118.

41 R. Hu, Y. Zhao, Y. Zhang, X. Wang, G. Li and M. Deng, Opto-mechano-thermo-sensitive allochroic luminescence based on coupled dual activators in tantalate towards multidimensional stimulus sensing, *Inorg. Chem. Front.*, 2023, **10**, 1225.

42 R. Hu, Y. Zhang, Y. Zhao, X. Wang, G. Li and M. Deng, Synergistic defect engineering and microstructure tuning in lithium tantalate for high-contrast mechanoluminescence of Bi^{3+}: toward application for optical information display, *Mater. Chem. Front.*, 2021, **5**, 6891–6903.

43 X. Geng, Y. Xie, S. Chen, J. Luo, S. Li, T. Wang, S. Zhao, H. Wang, B. Deng, R. Yu and W. Zhou, Enhanced local symmetry achieved zero-thermal-quenching luminescence characteristic in the Ca_2InSbO_6:Sm^{3+} phosphors for W-LEDs, *Chem. Eng. J.*, 2021, **410**, 128396.

44 Y. Jin, Y. Hu, Y. Fu, L. Chen, G. Ju and Z. Mu, Reversible colorless-cyan photochromism in Eu^{2+}-doped $Sr_3YNa(PO_4)_3F$ powders, *J. Mater. Chem. C*, 2015, **3**, 9435–9443.

45 J. Du, K. Li, R. V. Deun, D. Poelman and H. Lin, Near-infrared persistent luminescence and trap reshuffling in Mn^{4+} doped Alkali-earth metal tungstates, *Adv. Opt. Mater.Adv. Opt. Mater.*, 2021, **10**, 2101714.

46 T. Lyu and P. Dorenbos, Vacuum-referred binding energies of bismuth and lanthanide levels in $LiTaO_3$ perovskite: Toward designing energy storage phosphor for anti-counterfeiting, X-ray imaging, and mechanoluminescence, *Laser Photonics Rev.*, 2022, **16**, 2200304.

47 R. Chen, On the calculation of activation energies and frequency factors from glow curves, *J. Appl. Phys.*, 1969, **40**, 570.

48 T. Maldiney, A. Lecointre, B. Viana, A. Bessiere, M. Bessodes;, D. Gourier, C. Richard and D. Scherman, Controlling electron trap depth to enhance optical properties of persistent luminescence nanoparticles for in vivo imaging, *J. Am. Chem. Soc.*, 2011, **133**, 11810–11815.

49 H. Yuan, J. Li, W. Yang, Z. Zhuang, Y. Zhao, L. He, L. Xu, X. Liao, R. Zhu and L. Mai, Oxygen vacancy-determined highly efficient oxygen reduction in $NiCo_2O_4$/hollow carbon spheres, *ACS Appl. Mater. Interfaces*, 2018, **10**, 16410–16417.

50 Y. Song, H. Zhao, Y. Zi, J. Qiu, Z. Song, X. Bai, J. Liao and Z. Yang, X-ray-irradiation-induced discoloration and persistent radioluminescence for reversible dual-mode imaging and detection applications, *ACS Energy Lett.*, 2023, **8**, 2232–2240.

51 X. Lu, D. Wu, R. Li, Q. Li, S. Ye, Y. Xiang and G. Li, Hierarchical $NiCo_2O_4$ nanosheets@hollow microrod arrays for high-performance asymmetric supercapacitors, *J. Mater. Chem. A*, 2014, **2**, 4706.

52 G. Ou, Y. Xu, B. Wen, R. Lin, B. Ge, Y. Tang, Y. Liang, C. Yang, K. Huang, D. Zu, R. Yu, W. Chen, J. Li, H. Wu, L. Liu and Y. Li, Tuning defects in oxides at room temperature by lithium reduction, *Nat. Commun.*, 2018, **9**, 1302.